



HAL
open science

Metallic melt transport across castellated tiles

S. Ratynskaia, K. Paschalidis, K. Krieger, L. Vignitchouk, P. Talias, M. Balden, M. Faitsch, V. Rohde, Y. Corre, R.A. Pitts

► **To cite this version:**

S. Ratynskaia, K. Paschalidis, K. Krieger, L. Vignitchouk, P. Talias, et al.. Metallic melt transport across castellated tiles. Nuclear Fusion, 2024, 64 (3), pp.036012. 10.1088/1741-4326/ad219b . cea-04816600

HAL Id: cea-04816600

<https://cea.hal.science/cea-04816600v1>

Submitted on 3 Dec 2024









HAL is a multi-disciplinary open access archive for the deposit and dissemination of scientific research documents, whether they are published or not. The documents may come from teaching and research institutions in France or abroad, or from public or private research centers.

L'archive ouverte pluridisciplinaire **HAL**, est destinée au dépôt et à la diffusion de documents scientifiques de niveau recherche, publiés ou non, émanant des établissements d'enseignement et de recherche français ou étrangers, des laboratoires publics ou privés.



Distributed under a Creative Commons Attribution 4.0 International License

Metallic melt transport across castellated tiles

S. Ratynskaia^{1,*} , K. Paschalidis¹, K. Krieger² , L. Vignitchouk¹ , P. Talias¹ , M. Balden² , M. Faitsch² , V. Rohde², Y. Corre³ , R.A. Pitts⁴ , the ASDEX Upgrade Team^a and the EUROfusion MST1 Team^b

¹ Space and Plasma Physics—KTH Royal Institute of Technology, Teknikringen 31, 10044 Stockholm, Sweden

² Max-Planck-Institut für Plasmaphysik, Boltzmannstraße 2, D-85748 Garching, Germany

³ CEA, Institute for Research on Fusion by Magnetic Confinement, 13108 St-Paul-Lez-Durance, France

⁴ ITER Organization, Route de Vinon-sur-Verdon, CS 90 046, 13067 St Paul Lez Durance Cedex, France

E-mail: srat@kth.se

Received 25 October 2023, revised 26 December 2023

Accepted for publication 23 January 2024

Published 2 February 2024



Abstract

In future fusion reactors, extended melt pools in combination with strong plasma-induced accelerations, suggest that the metallic melt could reach the gaps between castellated plasma-facing components, potentially accompanied by profound changes in their mechanical response. The first results of a combined experimental and modelling effort to elucidate the physics of melt transport across gaps are presented. Transient melting of specially designed tungsten samples featuring toroidal gaps has been achieved in ASDEX Upgrade providing direct evidence of gap bridging. Detailed modelling with the MEMENTO melt dynamics code is reported. Empirical evidence and simulations reveal that the presence of gaps can be safely ignored in macroscopic melt motion predictions as well as that the re-solidification limited melt spreading facilitates gap bridging and leads to poor melt attachment. The findings are discussed in the context of ITER and DEMO.

Keywords: tungsten melting, melt edge wetting, melt gap bridging, large-scale melt motion, MEMENTO code

(Some figures may appear in colour only in the online journal)

1. Introduction

Damage of plasma-facing components (PFCs) under transient plasma heat loads remains a major challenge for the long-time operation of fusion reactors with metallic armour [1].

^a See Stroth *et al* 2022 (<https://doi.org/10.1088/1741-4326/ac207f>) for the ASDEX Upgrade Team.

^b See Labit *et al* 2019 (<https://doi.org/10.1088/1741-4326/ab2211>) for the EUROfusion MST1 Team.

* Author to whom any correspondence should be addressed.



Original Content from this work may be used under the terms of the [Creative Commons Attribution 4.0 licence](https://creativecommons.org/licenses/by/4.0/). Any further distribution of this work must maintain attribution to the author(s) and the title of the work, journal citation and DOI.

Substantial progress in the understanding of the evolution of surface deformation profiles, a result of the intricate interplay between macroscopic motion and heat transfer, has been achieved due to coordinated experimental [2–7] and modelling [8–12] efforts.

In future machines, extended PFC areas can be subject to intense heat loads [13, 14]. In combination with the strong plasma-induced acceleration, scenarios can be realized where melt reaches the gap between castellated PFCs. Modifications of the castellated design, e.g. by melt penetrating into the gaps, can have drastic consequences on the PFC mechanical response, especially under strong electromagnetic loads in the course of major disruptions [15].

The wetting of solids by liquids is a very complex phenomenon involving physical chemistry, wetting transitions,

long-range forces as well as fluid dynamics [16]. Concerning the latter aspects, the general picture is that spreading, driven by inertia and by capillary forces, is counteracted by viscous effects [16, 17]. In case of substantial temperature difference between the liquid and the solid substrate, re-solidification also hinders spreading [18, 19]. Therefore, the passage of the melt pools over PFC gaps or cracks depends on the melt speed, pool depth, liquid supply duration as well as the melt, PFC edge and inner gap wall temperatures. Naturally, these quantities are all dictated by the plasma heat loads and the PFC exposure scenarios. Thus far, rather limited modelling insight [20–22] and sparse tokamak evidence [5, 7, 23, 24] are available. There has been no systematic study dedicated to near-gap melt transport that addresses practical aspects of this problem: (1) the reliability of the deformation profile predictions of macroscopic melt motion simulations, with codes such as MEMENTO [9, 25], which ignore the presence of gaps. (2) The differentiation between the regimes of gap infiltration and gap bridging (limited penetration) on the basis of large-scale flow properties. (3) The stability of bridges against the stationary plasma and off-normal events.

Aiming to elucidate these aspects, dedicated tungsten (W) samples were designed that were simultaneously exposed to ELMing H-mode discharges in ASDEX upgrade (AUG). Two special types of samples were manufactured; a sample with a fully exposed leading edge (LE) at the upper half surface but flat below and a sample with a LE over the entire surface featuring a 0.5 mm toroidal gap. In this paper; the main experimental evidence are presented, the first simulations of the final deformation profile with the MEMENTO code are reported along with insights on the physical mechanisms behind the frozen melt pattern, the general properties of metallic melt flows after encountering an edge are analyzed on the basis of fluid dynamics. The practical aspects of gap crossing are discussed in the context of ITER and DEMO.

2. Experiment

2.1. Design and realization

The goals of the experiment are to evidence melt flow across an ITER-relevant toroidal gap as well as to realize melt splashing from a tile edge with all ejected material retained for post-mortem analysis. The former is achieved by manufacturing a LE that features a centered toroidal gap of $500\ \mu\text{m}$ width, as depicted in figure 1 (bottom). The gap is cut up to about half of the height of the sample. The latter is achieved by terminating a LE at half the sample length, as depicted in figure 1 (top). In both cases, the LE is machined in the middle of the sample. For convenience, they will be referred to as ‘step’ and ‘gap’ samples throughout the remaining text.

Both samples were simultaneously exposed to ELMing H-mode discharges at the outer divertor target plate using the divertor manipulator (DIM-II) system, for details see figures 1, 2 of [5]. Guided by the modelling of previous LE melting experiments in AUG [8] and the modelling of melt splashing from PFC edges [20], the targeted loading scenarios concerned

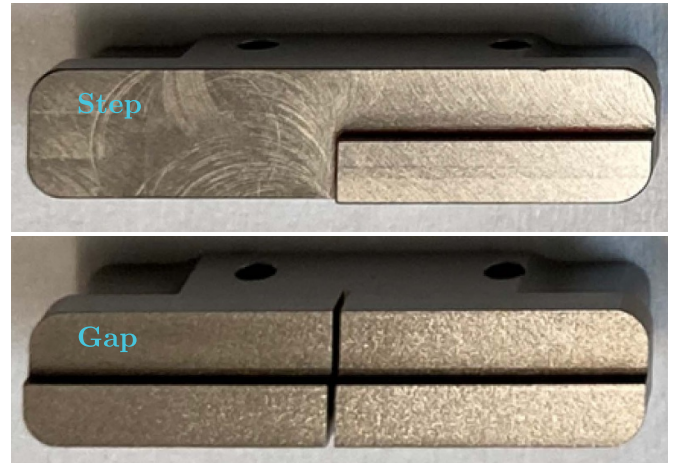


Figure 1. The manufactured ‘step’ (top) and ‘gap’ (bottom) samples; both $39\ \text{mm} \times 9\ \text{mm} \times 9\ \text{mm}$, with $1.1\ \text{mm}$ exposed leading edges (receiving the full parallel heat flux) machined in the middle of the samples. The toroidal gap (bottom sample) has $500\ \mu\text{m}$ width and $4\ \text{mm}$ depth.

the creation of melt pools away from the step or gap to enable a finite acceleration of the melt before it reaches the edge. The outer strike point (OSP) residence time on the sample was increased in successive steps and after each pulse the probe head was retracted for inspection aiming not to expose the samples post melting to avoid complications in interpretation and modelling.

After the reference discharges, the OSP was moved into the samples during nine shots #41317 – #41325. Visual sample inspection revealed that the initial discharges with pure ECRH heating did not deliver sufficient energy to melt the sample. Thus, for the last two exposures, #41324 & #41325, one source of NBI heating was added with a resulting doubling of the ELM frequency, from 50 to 100 Hz. The parameters for the last two shots are; $P = 2.415\ \text{MW}$ (NBI), $4.384\ \text{MW}$ (ECRH), $I_p = 1\ \text{MA}$ and $B_t = -2.5\ \text{T}$.

2.2. Main experimental features

In the course of discharge #41324, the gap sample was only superficially molten. In order to generate a sufficient melt volume for gap crossing, the OSP residence time was increased from 2.5 to 2.8 s in the following last discharge #41325. The resulting deformation profile is depicted in figure 2 (upper) and features an extended crater and amassment of the resolidified melt right after the gap. No profile peculiarities can be observed near the gap indicating that it did not induce particular perturbations to the melt flow. A side view of the sample (figure 2, lower) reveals that the melt crossed the gap forming a bridge without wetting the gap’s inner walls.

Owing to the slight ($\sim 1^\circ$) radial misalignment of DIM-II, the step sample received about 25% higher heat flux. As a consequence, already during discharge #41324 a significant melt pool was produced that splashed from the step edge, as

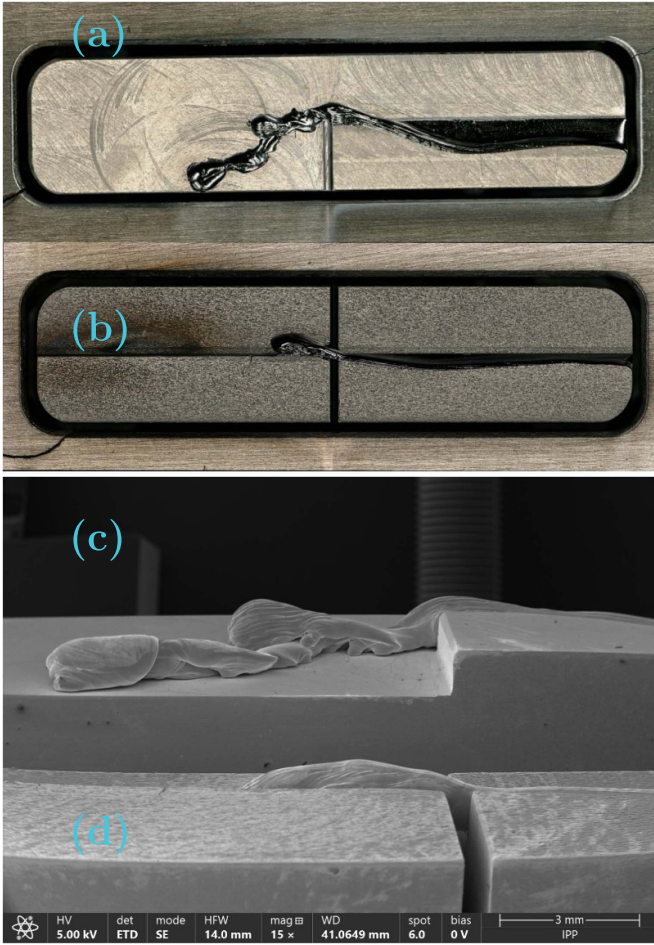


Figure 2. Top view of the exposed step (a) and gap (b) samples immersed in the tiles. Side view of the step (c) and gap (d) samples, zoom-in near the gaps. For more detailed view into the gap of the step sample refer to figure 7.

observed after retraction of the probe head. The sample was severely re-molten during the following discharge #41325, with fresh melt pools spilling over the re-solidified structures formed after the previous exposure, as observed in figure 2. This, combined with the fact that melt dynamics were affected by contact with the horizontal surfaces prevents the originally anticipated modelling attempts, similar to those conducted in [20, 21], since the melt was not in free fall. However, the evidence produced by the post-mortem analysis of this sample is crucial to the discussion about spreading and wetting, see section 4.1.

3. MEMENTO simulations

The primary objective is to reproduce the observed macroscopic melt motion and final deformation profile with the MEMENTO code in order to test whether the presence of the gap affects the large-scale dynamics of W melt pools.

The MEMENTO (METalic Melt Evolution in Next-step TOKamaks) code [9, 25, 26] is a new numerical implementation of the MEMOS-U physics model [8, 9, 11]. The

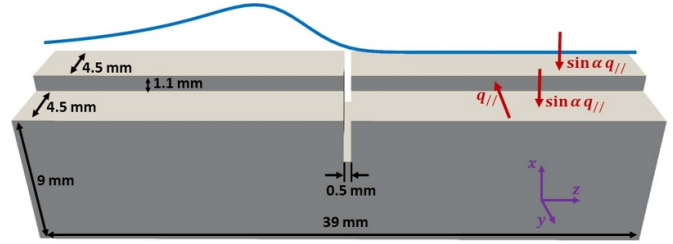


Figure 3. 3D geometry of the gap sample including the typical heat flux spatial profile.

model is based on the thermoelectric MHD equations coupled with heat transfer (including phase transitions); the electromagnetic field equations are formulated in the magnetostatic limit for uniform material composition and the Navier–Stokes equations are formulated within the shallow water approximation. MEMENTO relies on the AMReX open-source framework capabilities [27, 28] for computational efficiency. The code is adapted to handle complex domains and complicated loading scenarios, as exemplified here by the modelling of the sample featuring a gap and a step along with multiple plasmatweted surfaces.

In what follows, only the last discharge (#41325) of the exposure sequence is analyzed, since the preceding pulses did not lead to appreciable melting.

3.1. Heat flux loading

The heat flux onto the samples has been reconstructed from the standard IR thermography diagnostic in a sector toroidally $\sim 180^\circ$ away from the exposure position [4, 5]. The experimental heat flux from discharge #41325 has been post-processed in a manner similar to [10]. More specifically, unphysical negative values have been substituted with an analytical fit of the inter-ELM spatial profile recovered by the IR data and a flux reduction coefficient (0.75) has been introduced to ensure the preservation of the overall deposited energy. Finally, to best match the observations, the heat flux has been shifted by 4 mm along the sample (well within the ~ 1 cm uncertainty) and has been increased by 27% (again within the experimental underestimation of the IR-recovered power flux), see [10], for a detailed discussion. The field-parallel heat flux characteristic maximum intra- and inter-ELM values are $\sim 900 \text{ MW m}^{-2}$ and $\sim 100 \text{ MW m}^{-2}$, respectively, with ELM frequency of $\sim 100 \text{ Hz}$ and ELM duration $< 3 \text{ ms}$.

The 3D geometry of the gap sample is shown in figure 3 together with the characteristic spatial profile of the heat flux. Such a profile, ‘tailored’ by the OSP position, reflects the experimental aim of creating melt pools away from the gap edge, as discussed in section 2.1. The LE receives the full parallel heat flux, while, within the optical approximation, the upper and lower top surfaces receive the parallel flux reduced by $\sin \alpha$, with $\alpha = 2.8^\circ$ the magnetic field inclination angle with respect to the surface tangent. The sample is loaded for 3.12 s, which includes the steady OSP as well as the sweep-in

and sweep-out. The total simulation time is 3.2 s so that complete re-solidification is accommodated.

3.2. Thermal response

In the MEMENTO implementation, the gap is emulated by introducing an artificial solid W region of zero thermal conductivity which acts as an insulating layer. The underlying gap free surfaces are naturally subject to evaporative and radiative cooling.

As discussed in section 2, in contrast to the earlier AUG LE melting experiments [8, 9, 11] where the flux intersecting area lied at a corner of the sample, the LE is now machined in the middle of the top surface. Such LE position implies an effective cooling channel for the wetted surface via heat diffusion to the bulk that affects the thermal response and, in turn, the macroscopic melt motion.

Moreover, the gap alters the thermal response since the two halves are subject to different heat fluxes. Insulation hinders heat diffusion from one half to the other, thus promoting melt generation on the hotter half (left in figure 3). More specifically, the temperature difference between the two gap LE corners is ~ 2000 K prior to bridging.

Sample melting first occurs at ~ 1 s, followed by consecutive melting events induced by each ELM. These transient pools are short-lived (< 10 ms) with instantaneous melt depths h reaching $\sim 80 \mu\text{m}$. It is noted that these are typical values; their range depends on the fluctuating ELM heat flux spatiotemporal parameters. The melt surface temperature does not exceed the W melting point by more than 300–400 K. For the LE geometry and for plasma densities of $1.5 \times 10^{19} \text{ m}^{-3}$, the escaping thermionic current density is $\sim 4 \text{ MA m}^{-2}$ in the inter-ELM period and reaches up to $\sim 10 \text{ MA m}^{-2}$ during intra-ELM periods [29–31].

3.3. Melt dynamics and deformation profiles

Similar to the earlier W LE melt experiments [8, 9, 11], Lorentz acceleration driven by thermionic emission dominates and is responsible for the main melt displacement along the sample. As pointed out in [10], Marangoni flows (thermo-capillary effects) contribute to motion in the direction perpendicular to the Lorentz force. In the modelling results presented here both acceleration mechanisms are included. Gravity points downwards along the tile surface which has a vertical inclination of 15° and is negligible, being $\sim 20\times$ weaker than the $J \times B$ force density.

The final deformation profile amounts to the accumulation of individual transient pool displacements as it is typical of ELM-induced melting events [8, 9, 11]. The melt velocities v do not exceed 0.2 m s^{-1} , given the modest pool depth of several tens of μm and the $1/h^2$ scaling of viscous damping. Such slow motion, further impeded by the prompt re-solidification upon contact with the much colder surface across the gap, results in a melt pile-up in the vicinity of the crater edge that nearly coincides with the gap edge.

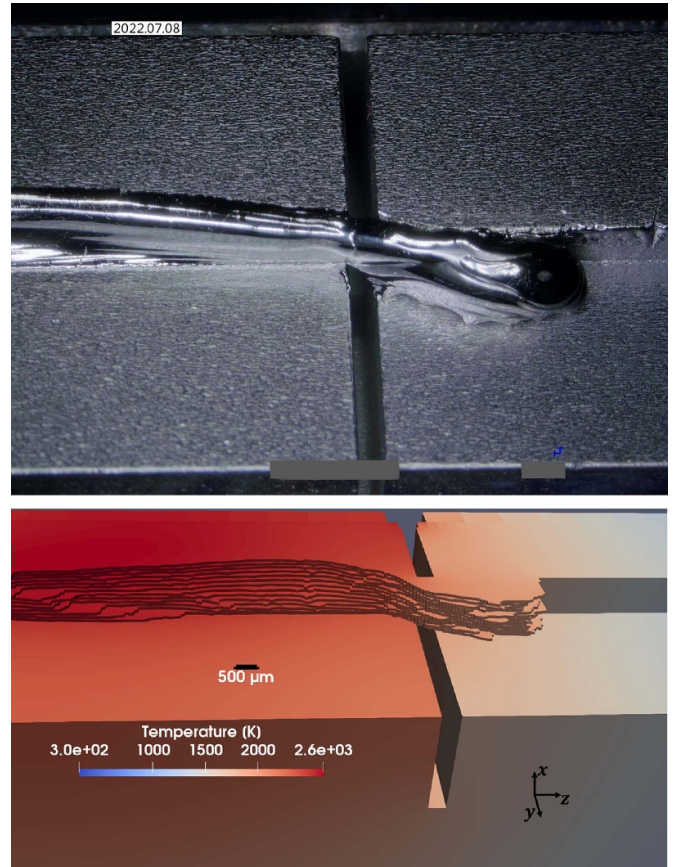


Figure 4. (Upper) Zoomed-in final deformation profile near the gap. (Lower) MEMENTO simulation results: 3D computational domain with the *re-solidified* melt 70 ms after heat flux termination.

A zoomed-in image in the vicinity of the gap is shown in figure 4 along with the MEMENTO simulation result. It is evident that the simulations capture all features of the crater and displaced re-solidified melt exceptionally well. In particular, the spread of the melt over the lower horizontal surface perpendicular to the LE is reproduced thanks to the inclusion of the thermo-capillary effects which push the melt from the hottest edge down to the colder areas. The only aspect of the experimental profile which cannot be faithfully reproduced concerns the melt bulging above the LE. This feature is a 3D effect where the surface tension establishes a finite curvature of the melt edge. Naturally this cannot be treated within the shallow water approximation which constitutes the backbone of the MEMENTO code. It is stressed that this limitation specifically concerns the melt pool right at the PFC edges (as well as the molten edges) where the geometry is truly 3D. Elsewhere, the surface tension can be modelled similarly to thin films [32, 33], as recently implemented in MEMENTO [25, 26].

The close matching of the crater and the material pile-up extensions can be also deduced by the comparison of the sample profilometry with the MEMENTO deformation profile that is presented in figure 5. Another important figure of merit is the displaced melt volume, which is also accurately

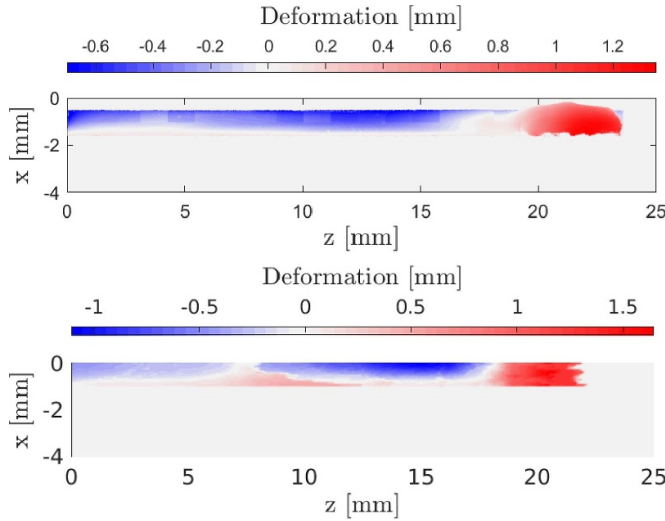


Figure 5. (Upper) Profilometry of the sample—view into the leading edge. (Lower) MEMENTO modelling results: deformation of the leading edge. For the coordinate system refer to figure 3.

reproduced, with 4.7 mm^3 in the experiment and 4.8 mm^3 in the simulations.

4. Wetting dynamics and gap bridging

In what follows, we shall analyze the central role of solidification in determining the properties of metallic melt flows after encountering an edge. In particular, we shall focus on experimental evidence of melt spreading dynamics on the cold solid surfaces across gaps and past step edges. Furthermore, we shall discuss the fact that the melt was observed to bridge the gap sample without any visible infiltration into the gap itself, despite its low velocity. Finally, with the help of past experimental results and simulation efforts, we will attempt to formulate a more general picture of wetting and bridging for the parameter regimes that are relevant to transient PFC melting in fusion devices.

4.1. Spreading limited by solidification

Examples of the contacts formed between the displaced W melt and cold W surfaces downstream of the gap and step samples are displayed in figure 6. It can be discerned that the W melt does not significantly spread over the underlying W solid. This is particularly evident in figures 6(b) and (c), where the apparent contact angles between the re-solidified melt and the underlying surface are of the order of 90° and above, suggesting a low wettability [16]. Moreover, a fragment of re-solidified melt, see figure 6(d), fell off the step sample in the course of the post-mortem analysis, indicating poor attachment. Similar evidence had been obtained in an earlier AUG experiment, where the solidified W melt, that spilled from an exposed LE, was detached by plasma-induced forces in a subsequent pulse, ultimately causing a disruption [23].

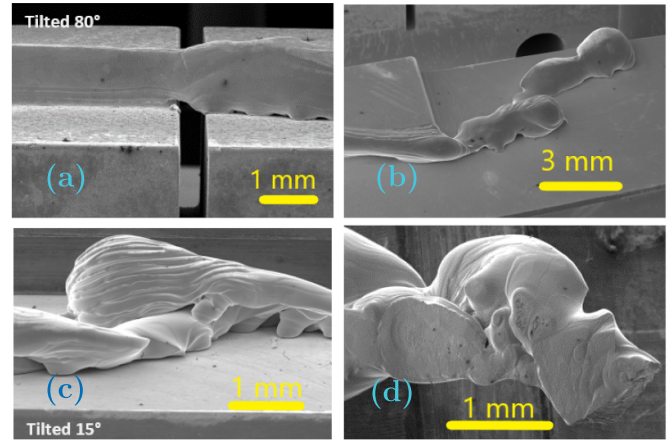


Figure 6. Examples of poor melt attachment. The tilted SEM images aim for enhanced visualisation of the melt contact with the surface and of the capillary waves. (a) Gap sample. (b) Step sample. (c) Zoomed-in step sample. (d) Piece of re-solidified melt that detached from the step sample in the course of the post-mortem analysis; the visible flat region was originally in contact with the sample.

The above observations are in apparent contradiction with the known fact that liquid metals tend to exhibit excellent wettability on their own solids, as a consequence of their high surface energies and strong interfacial bonding properties [16, 34]. In isothermal conditions, wetting dynamics result from the balance between capillary forces, which promote liquid spreading towards a small equilibrium contact angle in case of metals, and inertial/viscous effects which tend to resist fluid motion [16, 35]. However, in the presence of large temperature differences between the two phases, the solidification can become the dominant momentum sink. Its relative importance can be quantified by comparing the characteristic time scale $\tau_{\text{vis}} = \rho h^2 / \mu$ associated with viscous stresses in a liquid layer of thickness h (ρ is the mass density, μ the dynamic viscosity) with the characteristic time τ_{sol} required to freeze that liquid layer. Considering a characteristic conduction heat flux $k\Delta T/h$, where k denotes the thermal conductivity and ΔT the temperature difference between phases, τ_{sol} can be estimated as $\rho h^2 \Delta h_f / k\Delta T$, with Δh_f the latent heat of fusion, provided that the time required to cool the liquid down to its melting point is not much larger than the duration of the phase transition at constant temperature. Hence, solidification dominates over the viscosity when $\tau_{\text{sol}} \ll \tau_{\text{vis}}$. It is evident that the criterion depends exclusively on material properties and the temperature difference, since the layer thickness h cancels out. This criterion can be conveniently expressed in terms of the dimensionless Prandtl and Stefan numbers as $\text{Pr} \ll \text{Ste}$, where $\text{Pr} = \mu c_p / k$ and $\text{Ste} = c_p \Delta T / \Delta h_f$, with c_p denoting the specific heat capacity. Moreover, the assumption on the relative smallness of the liquid cool-down time corresponds to $\text{Ste} \lesssim 1$.

The wetting dynamics can differ significantly from the isothermal case, when $\text{Pr} \ll \text{Ste} \lesssim 1$. In fact, no complete theoretical picture exists, and the microscopic physics near the contact line are still debated [19, 36, 37]. Nevertheless, relevant experimental observations of wetting are available

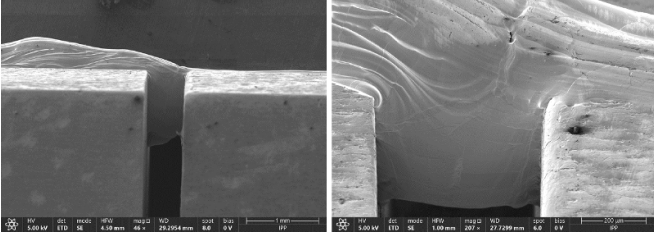


Figure 7. Zoomed-in images of the bridged gap sample. The gap width of $500\ \mu\text{m}$ can be employed as a reference length scale. Note that, in these images, the melt flow is directed from right to left, i.e. in the opposite direction compared to the previous figures.

in the literature, which reveal that solidification can result in large apparent contact angles even in good wettability conditions [17, 18, 37]. In order to relate our experimental data to these published results, which mainly concern spherical droplets instead of liquid layers, we consider a melt pool with a thickness h and an extent L along the direction of spreading. The characteristic time scale that arises from capillary forces and liquid inertia can be estimated as $\tau_{\text{cap}} = \sqrt{\rho h L^2 / \gamma}$, where γ is the surface tension. Therefore, the ratio of $\tau_{\text{sol}} / \tau_{\text{cap}}$ can be expected to constitute a reliable dimensionless metric on which to base our comparisons. In [37], solidification-limited spreading is reported with final contact angles above 90° under conditions corresponding to $\tau_{\text{sol}} / \tau_{\text{cap}} \simeq 10$. Thus, it can be postulated that poor apparent wetting should arise for comparable or smaller values, i.e. when

$$\frac{h}{L} \frac{\text{Pr}}{\text{Ste Oh}} \lesssim 10, \quad (1)$$

where the Ohnesorge number is defined by $\text{Oh} = \mu / \sqrt{\rho h \gamma}$. Considering the thermophysical properties of liquid W at 3800 K [38]; $\rho = 16185\ \text{kgm}^{-3}$, $\mu = 7.6\ \text{mPas}$, $\gamma = 2.45\ \text{Nm}^{-1}$, $k = 68\ \text{Wm}^{-1}\text{K}^{-1}$, $c_p = 279\ \text{Jkg}^{-1}\text{K}^{-1}$, $\Delta h_f = 280\ \text{kJkg}^{-1}$, along with the MEMENTO simulation results; $h = 100\ \mu\text{m}$, $L = 1\ \text{mm}$ and $\Delta T = 2000\ \text{K}$, we obtain $\text{Pr} = 0.03$, $\text{Ste} = 2$ and $\text{Oh} = 0.004$. Therefore, the criteria for solidification-limited spreading are fulfilled in the conditions relevant to figure 6, consistent with the observed poor effective wetting and the fact that the melt did not noticeably spread transversely when moving upon cold surfaces. In fact, the strong impact of re-solidification on wetting dynamics is also evidenced by the presence of multiple surface ridges, that are especially visible on figure 6(c), which correspond to capillary waves that are essentially frozen in place before they can mediate the wetting process. Similar observations have indeed been reported in multiple fusion-relevant melting experiments [39–41].

4.2. Gap infiltration and bridging

The post-exposure morphology of the gap sample, see figure 7, strongly suggests that the motion of the melt layer was essentially unaffected by the presence of the gap. In particular, no melt infiltration can be discerned upon the inner gap surfaces.

However, when ignoring heat transfer effects, a comparative time scale analysis similar to the above suggests that capillary processes dominate both the upstream melt inertia and the Lorentz acceleration. Indeed, for isothermal conditions in the vicinity of the right-angle gap edge, surface tension acts on a $\tau_{\text{cap}} = \sqrt{\rho h^3 / \gamma}$ time scale, the characteristic time scale associated with inertial motion at the upstream velocity v is $\tau_{\text{vel}} = h/v$ and the time scale associated with the volumetric Lorentz force F is given by $\tau_{\text{acc}} = \sqrt{\rho h / F}$. The ratios of the three time scales involve the Weber and Bond numbers, defined by $\text{We} = (\tau_{\text{cap}} / \tau_{\text{vel}})^2 = \rho h v^2 / \gamma$ and $\text{Bo} = (\tau_{\text{cap}} / \tau_{\text{acc}})^2 = F h^2 / \gamma$. Using the same material properties as in section 4.1, together with $h = 100\ \mu\text{m}$, $v = 0.1\ \text{ms}^{-1}$, $F = 3\ \text{MNm}^{-3}$ emerging from the MEMENTO simulations, yields $\text{We} = 0.007$ and $\text{Bo} = 0.01$. Therefore, in absence of heat transfer effects, in contradiction to the experimental evidence, the melt flow would be expected to remain attached to the solid underneath by propagating along the inner gap wall as long as the upstream melt supply is maintained.

As in section 4.1, the viscous effects can be neglected in a first order approximation given that $\text{Pr} \ll \text{Ste} \lesssim 1$ with $\text{Ste} = 0.5$ resulting from using $\Delta T = 500\ \text{K}$ for the temperature difference between the upstream melt layer and inner gap wall, as revealed by the MEMENTO simulations. However, the applicability of equation (1), derived for spreading on flat surfaces across the main direction of motion, is dubious since the sharp edge geometry implies that the melt thickness and extent are badly defined quantities. In fact, wetting processes on the inner gap wall cannot be initiated before a threshold melt volume is made available by the upstream flow. Hence, the most relevant comparison concerns the inertial and solidification time scales, whose ratio is given by $\tau_{\text{sol}} / \tau_{\text{vel}} = \text{Pe} / \text{Ste}$, where the Péclet number is defined by $\text{Pe} = \rho c_p h v / k$. The low melt velocities expected in the gap sample correspond to $\text{Pe} = 0.7$, i.e. to $\text{Pe} \sim \text{Ste}$. In other words, a large fraction of the melt volume flowing around the edge may re-solidify before completing the 90° rotation required to penetrate into the gap.

To our knowledge, dedicated controlled experiments focusing on solidification-limited wetting dynamics on solid edges have not been reported in the literature. Additional insight can be gained from earlier tokamak melt studies. In particular, post-mortem surveys of beryllium (Be) flows in the vicinity of PFC edges have been performed in JET in the context of disruption-induced melt events [7]. In contrast to the present AUG exposures, the JET melt layers fill the castellation gaps, as illustrated in the upper panel of figure 8, and their motion is visibly affected by right-angle edges, resulting in waterfall-like structures [7, 40]. These observations were successfully reproduced by dedicated Navier–Stokes simulations [20, 22], whose results are exemplified in the lower panel of figure 8. The simulations demonstrated that the main competition in such conditions concerns inertia and surface tension, as encoded in the values of We . Solidification, though a non-negligible damping mechanism in the simulations, was not found to prevent melt motion along the downstream edge regions.

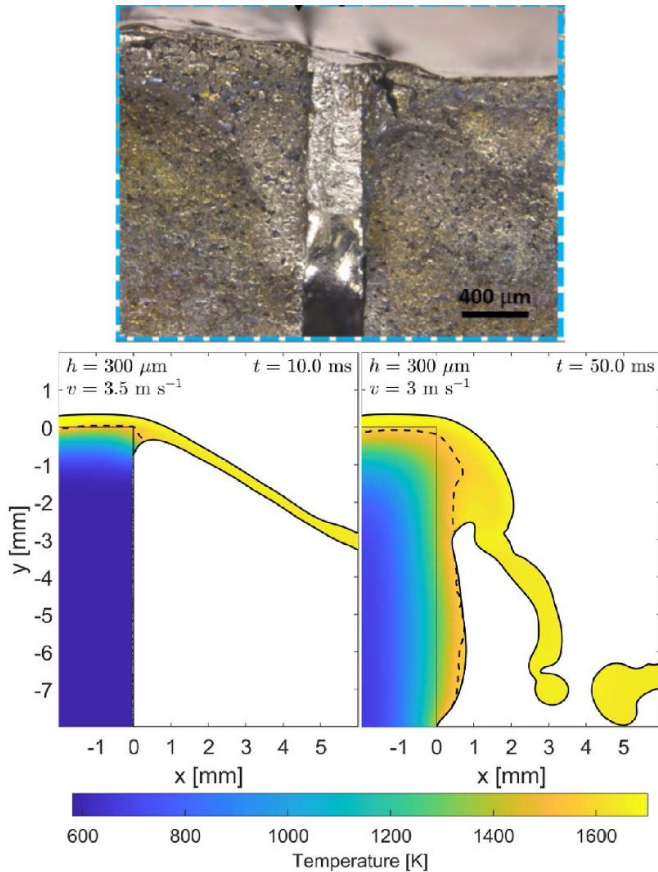


Figure 8. Upper; JET Be melting event during the current quench, reproduced after reproduced courtesy of IAEA. Figure from [7]. Copyright EURATOM 2019. Lower; simulations of liquid Be flow over the right corner by specialized ANSYS set-ups [42], reproduced after reproduced from [22]. The Author(s). CC BY 4.0.

By comparing the various dimensionless numbers that characterize the melt flows observed near PFC edges in JET and AUG, the following parameter regimes emerge. (i) In the JET disruption-induced Be melt events, the liquid layers move with a relatively high velocity, which leads to $We \sim 1$ and $Pe \gg Ste$, since the melt characteristics obtained from modelling studies [8] yield $We = 3$, $Pe = 56$ and $Ste = 2$. In this regime, edge dynamics are mainly governed by the balance between inertia and surface tension. Critical values of We are expected to distinguish between attached flows (melt mainly spreads on the downstream edge wall) and jetting flows (most melt detaches from the underlying solid) [20]. Unless $We \gg 1$, wetting dynamics may still develop near the edge and lead to a small but non-negligible melt propagation along the downstream surface. (ii) In the AUG ELM-induced W melt events, the liquid layers are relatively slow, which translates to $We \ll 1$ and $Pe \sim Ste$. In this regime, the main relevant balance arises between inertia and solidification; critical values of the ratio Pe/Ste are expected to distinguish between attached flows (significant melt spreading) and bridging flows (no noticeable wetting of the downstream wall). In the latter case, the newly frozen metal may create a thin ramp-like

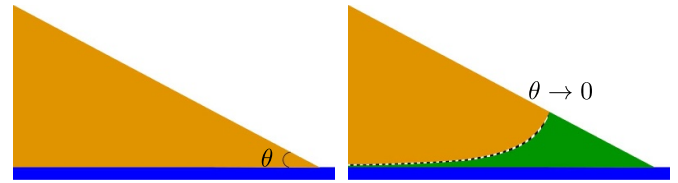


Figure 9. Left: an initial contact angle θ between incoming melt (orange) and the original solid substrate (blue). Right: modified contact geometry in the presence of an upstream-propagating solidification front (dashed curve); the freshly solidified region (green) results in a zero effective contact angle, defined as the supplement of the angle between the liquid–vapour and solid–vapour interfaces.

structure, extending the upstream wall and thereby facilitating further melt flow away from the edge. Even though the formation of such structures on the AUG gap sample remains somewhat speculative in view of the experimental evidence, it is supported by simulation results. In the lower left figure 8 panel which corresponds to a high-velocity jetting layer, the re-solidified region near the edge exhibits a protruding wedge-like shape, whose further growth is prevented by the continuous convective supply of thermal energy upstream of the corner. In low-velocity regimes, such wedges can in principle keep extending along the main flow direction, as long as melt supply is maintained and heat conduction into the solid bulk remains efficient enough to prevent their re-melting. It is also noted that these simulation results exemplify how the presence of temperature gradients along the downstream wall leads to a preferential propagation of the solidification front against the direction of spreading, which may produce effectively perfect wetting configurations, as sketched in figure 9.

5. Summary and conclusions

The design, realization and modelling of the first controlled experiment of melt transport across PFC gaps has been reported. The excellent quantitative matching of the experimental deformation profile by the MEMENTO simulations convincingly demonstrates that gaps can be ignored when modelling macroscopic melt motion, despite a lack of detailed knowledge of gap melt infiltration or bridge formation. The reason is that when the gap dimensions are small compared to those of the melt pool, the perturbations of large-scale flow are insignificant. This is of high practical value for simulations of large-scale melting under disruption loads in ITER or DEMO and of ELM-induced divertor monoblock melting in ITER.

The post-mortem analysis of both exposed samples reveals apparent poor wetting and the weak attachment of re-solidified melt. This is a consequence of re-solidification which limits melt spreading, preventing complete wetting so that small equilibrium contact angles are not realized. This interpretation is strongly supported by the observation of frozen capillary waves and has been corroborated by time scale estimates utilizing thermal response and large-scale flow input from MEMENTO simulations. Less conclusive evidence of

limited melt spreading had been earlier encountered in different fusion-relevant scenarios. Frozen capillary waves were first observed in experiments with adhered W dust clusters subject to the transient heat flux of the Pilot-PSI linear plasma device [39, 43] and can even be discerned in a molten W tile exposed in JET [40, 41].

Another important experimental result concerns the evidence of gap bridging without wetting of the inner gap walls. This is also a consequence of re-solidification which prevents the melt from revolving around the corner by altering the sharp edge topology. A contradistinction with the molten Be infiltration of the JET castellated PFCs [7], highlights that the details of gap wetting are sensitive to the melt speed, pool depth, melt life time as well as to the liquid metal and inner wall temperatures. This implies that the bridging evidence presented herein is not necessarily relevant to disruption scenarios in ITER and DEMO, where larger wetted areas, deeper melting and faster pools might lead to full gap infiltration. Moreover, this experiment featured a dramatically colder half sample due to the incident heat flux discrepancy given the rapidly decaying profile and due to the thermal separation offered by the deep gap. Prompt bridge freezing due to contact with the surface across the gap will not take place in case of adjacent ITER divertor monoblocks wetted by ELMs, whose decay length by far exceeds the monoblock dimensions.


Future efforts to further improve our understanding of gap melt infiltration will be directed towards both the experimental and the computational fronts. In particular, a planned experiment in the WEST tokamak, where ultra-shallow and slow melt pools will be generated close to a W divertor monoblock edge, should assist in elucidating the near-gap dynamics of sustained pools. As far as modelling is concerned, the macroscopic MEMENTO simulations should be supplemented by simulations capable of resolving small-scale dynamics, as done with specialized ANSYS set-ups in [20]. However, while such simulations were feasible in the regime of high-speed convection-dominated flows, low-speed scenarios dominated by heat diffusion and re-solidification are expected to be significantly more challenging. The difficulty stems from the fact that inlet boundary conditions cannot be imposed consistently upstream of the gap, hence large melt volumes have to be included in the simulation domain, which implies a dramatic increase of the computational cost.

Acknowledgments

S R & P T acknowledge the financial support of the Swedish Research Council under Grant No. 2021-05649. The work has also been performed within the framework of the EUROfusion Consortium, funded by the European Union via the Euratom Research and Training Programme (Grant Agreement No. 101052200—EUROfusion). The views and opinions expressed are however those of the authors only and do not necessarily reflect those of the European Union, the European Commission or the ITER Organization. The European Union, European Commission or ITER Organization cannot be held responsible for them. MEMENTO simulations were

enabled by resources provided by the National Academic Infrastructure for Supercomputing in Sweden (NAISS) and the Swedish National Infrastructure for Computing (SNIC) at the NSC (Linköping University) partially funded by the Swedish Research Council through Grant Agreement Nos. 2022-06725 and 2018-05973.

ORCID iDs

S. Ratynskaia  <https://orcid.org/0000-0002-6712-3625>
 K. Krieger  <https://orcid.org/0000-0003-0427-8184>
 L. Vignitchouk  <https://orcid.org/0000-0001-7796-1887>
 P. Toliás  <https://orcid.org/0000-0001-9632-8104>
 M. Balden  <https://orcid.org/0000-0002-8755-9370>
 M. Faitsch  <https://orcid.org/0000-0002-9809-7490>
 Y. Corre  <https://orcid.org/0000-0002-6566-6116>
 R.A. Pitts  <https://orcid.org/0000-0001-9455-2698>

References

- [1] Pitts R.A. et al 2017 Physics conclusions in support of ITER W divertor monoblock shaping *Nucl. Mater. Energy* **12** 60
- [2] Corre Y. et al 2023 Testing of ITER-like plasma facing units in the WEST tokamak: progress in understanding heat loading and damage mechanisms *Nucl. Mater. Energy* **37** 101546
- [3] Corre Y. et al 2021 Sustained W-melting experiments on actively cooled ITER-like plasma facing unit in WEST *Phys. Scr.* **96** 124057
- [4] Krieger K. et al 2017 Investigation of transient melting of tungsten by ELMs in ASDEX Upgrade *Phys. Scr.* **T170** 014030
- [5] Krieger K. et al 2018 Experiments on transient melting of tungsten by ELMs in ASDEX Upgrade *Nucl. Fusion* **58** 026024
- [6] Coenen J.W. et al 2015 ELM-induced transient tungsten melting in the JET divertor *Nucl. Fusion* **55** 023010
- [7] Jepsen I. et al 2019 Beryllium melting and erosion on the upper dump plates in JET during three ITER-like wall campaigns *Nucl. Fusion* **59** 086009
- [8] Ratynskaia S., Thorén E., Toliás P., Pitts R.A., Krieger K., Vignitchouk L. and Iglésias D. 2020 Resolidification-controlled melt dynamics under fast transient tokamak plasma loads *Nucl. Fusion* **60** 104001
- [9] Ratynskaia S., Thorén E., Toliás P., Pitts R.A. and Krieger K. 2021 The MEMOS-U macroscopic melt dynamics code - benchmarking and applications *Phys. Scr.* **96** 124009
- [10] Ratynskaia S., Paschalidis K., Toliás P., Krieger K., Corre Y., Balden M., Faitsch M., Grosjean A., Tichit Q. and Pitts R.A. 2022 Experiments and modelling on ASDEX Upgrade and WEST in support of tool development for tokamak reactor armour melting assessments *Nucl. Mater. Energy* **33** 101303
- [11] Thorén E., Ratynskaia S., Toliás P. and Pitts R.A. 2021 The MEMOS-U code description of macroscopic melt dynamics in fusion devices *Plasma Phys. Control. Fusion* **63** 035021
- [12] Thorén E., Ratynskaia S., Toliás P., Pitts R.A., Krieger K., Komm M. and Balden M. 2018 MEMOS 3D modelling of ELM-induced transient melt damage on an inclined tungsten surface in the ASDEX Upgrade outer divertor *Nucl. Mater. Energy* **17** 194
- [13] Coburn J., Thoren E., Pitts R.A., Anand H., Lehnen M., Kos L., Brank M., Ratynskaia S. and Toliás P. 2020 First wall energy deposition during vertical displacement events on ITER *Phys. Scr.* **T171** 014076

- [14] Coburn J. *et al* 2022 Energy deposition and melt deformation on the ITER first wall due to disruptions and vertical displacement events *Nucl. Fusion* **62** 016001
- [15] Lehnen M. *et al* 2015 Disruptions in ITER and strategies for their control and mitigation *J. Nucl. Mater.* **463** 39
- [16] de Gennes P.G. 1985 Wetting: statistics and dynamics *Rev. Mod. Phys.* **57** 827
- [17] Pasandideh-Fard M., Qiao Y.M., Chandra S. and Mostaghimi J. 1996 Capillary effects during droplet impact on a solid surface *Phys. Fluids* **8** 650
- [18] Pasandideh-Fard M., Bhola R., Chandra S. and Mostaghimi J. 1998 Deposition of tin droplets on a steel plate: simulations and experiments *Int. J. Heat Mass Transfer* **41** 2929
- [19] Gielen M.V., Ruiter R.D., Koldewij R.B.J., Lohse D., Snoeijer J.H. and Gelderblom H. 2020 Solidification of liquid metal drops during impacts *J. Fluid Mech.* **883** A32
- [20] Vignitchouk L., Ratynskaia S., Pitts R.A. and Lehnen M. 2022 Simulations of liquid metal flows over plasma-facing component edges and application to beryllium melt events in JET *Nucl. Fusion* **62** 036016
- [21] Vignitchouk L., Ratynskaia S., Pitts R.A. and Lehnen M. 2023 Beryllium melt instabilities and ejection during unmitigated current quenches in ITER *Nucl. Fusion* **63** 016004
- [22] Ratynskaia S., Vignitchouk L. and Toliás P. 2022 Modelling of dust generation, transport and remobilization in full-metal fusion reactors *Plasma Phys. Control. Fusion* **64** 044004
- [23] Coene J.W., Krieger K., Lipschultz B., Dux R., Kallenbach A., Lunt T., Mueller H.W., Potzel S., Neu R. and Terra A. 2013 Evolution of surface melt damage, its influence on plasma performance and prospects of recovery *J. Nucl. Mater.* **438** S27
- [24] Tichit Q. *et al* 2023 Infrared detection of tungsten cracking on actively cooled ITER-like component during high power experiment in WEST *Nucl. Mater. Energy* **37** 101537
- [25] Paschalidis K., Ratynskaia S., Lucco Castello F. and Toliás P. 2023 Melt dynamics with MEMENTO—code development and numerical benchmarks *Nucl. Mater. Energy* **37** 101545
- [26] Paschalidis K., Lucco Castello F., Ratynskaia S., Toliás P. and Brandt L. 2024 The MEMENTO code for modelling of macroscopic melt motion in fusion devices *Int. J. Numer. Methods Fluids* (submitted)
- [27] AMReX development team (available at: <https://amrex-codes.github.io/amrex/>)
- [28] Zhang W. *et al* 2019 AMReX: a framework for block-structured adaptive mesh refinement *J. Open Source Softw.* **4** 1370
- [29] Komm M., Ratynskaia S., Toliás P., Cavalier J., Dejarnac R., Gunn J.P. and Podolnik A. 2017 On thermionic emission from plasma-facing components in tokamak-relevant conditions *Plasma Phys. Control. Fusion* **59** 094002
- [30] Komm M., Toliás P., Ratynskaia S., Dejarnac R., Gunn J.P., Krieger K., Podolnik A., Pitts R.A. and Panek R. 2017 Simulations of thermionic suppression during tungsten transient melting experiments *Phys. Scr.* **T170** 014069
- [31] Komm M., Ratynskaia S., Toliás P. and Podolnik A. 2020 Space-charge limited thermionic sheaths in magnetized fusion plasmas *Nucl. Fusion* **60** 054002
- [32] Bertozzi A.L. and Brenner M.P. 1997 Linear stability and transient growth in driven contact lines *Phys. Fluids* **9** 530
- [33] Kondic L. and Diez J. 2001 Pattern formation in the flow of thin films down an incline: constant flux configuration *Phys. Fluids* **13** 3168–84
- [34] Eustathopoulos N., Nicholas M. and Drevet B. 1999 *Wettability at High Temperatures* (Pergamon)
- [35] Bianca A.-L., Clanet C. and Quéré D. 2004 First steps in the spreading of a liquid droplet *Phys. Rev. E* **69** 016301
- [36] Schiaffino S. and Sonin A.A. 1997 Molten droplet deposition and solidification at low Weber numbers *Phys. Fluids* **9** 3172–87
- [37] de Ruiter R., Colinet P., Brunet P., Snoeijer J.H. and Gelderblom H. 2017 Contact line arrest in solidifying spreading drops *Phys. Rev. Fluids* **2** 043602
- [38] Toliás P. 2017 Analytical expressions for thermophysical properties of solid and liquid tungsten relevant for fusion applications *Nucl. Mater. Energy* **13** 42
- [39] Ratynskaia S. *et al* 2016 Interaction of adhered metallic dust with transient plasma heat loads *Nucl. Fusion* **56** 066010
- [40] Matthews G.F. *et al* 2016 Melt damage to the JET ITER-like wall and divertor *Phys. Scr.* **T167** 014070
- [41] Coenen J.W. *et al* 2017 Transient induced tungsten melting at the Joint European Torus JET *Phys. Scr.* **T170** 014013
- [42] Vignitchouk L., Khodak A., Ratynskaia S. and Kaganovich I. 2020 Numerical benchmark of transient pressure-driven metallic melt flows *Nucl. Mater. Energy* **25** 100826
- [43] Ratynskaia S. *et al* 2017 Tungsten dust remobilization under steady-state and transient plasma conditions *Nucl. Mater. Energy* **12** 569